Advances in Technology Innovation, vol. 10, no. 3, 2025, pp. 238-253

A Modified Exponential Model for Predicting the Fatigue Crack Growth Rate in a Pipeline Steel Under Pure Bending

Sergei Sherbakov[1], Pawan Kumar[1,*], Daria Podgayskaya[1], Pavel Poliakov[2], Vasilii Dobrianskii[2], Vishwanatha H M[3]

[1]Joint institute of mechanical engineering of the National Academy of Sciences of Belarus, Minsk, Belarus

[2]Moscow Aviation Institute (National Research University), Moscow, Russia

[3]Department of Mechanical and Industrial Engineering, Manipal Institute of Technology, Manipal Academy of Higher Education, Manipal, India

Received 08 October 2024; received in revised form 09 February 2025; accepted 13 March 2025

DOI: https://doi.org/10.46604/aiti.2024.14372

Abstract

The present work proposes a fatigue crack growth rate (FCGR) model for steel pipelines subjected to sinusoidal loading using a modified exponential function. The modification in the exponential function is made for the non-dimensional parameter using the stress intensity range (ΔK) as the crack driving force. The acceptable values of ΔK for FCGR in stage-I ranged between 17.45-20.46 $MPa\sqrt{m}$, between 20.46-21.41 $MPa\sqrt{m}$ for stage-II, and between 21.41-21.98 $MPa\sqrt{m}$ for stage-III. A new correlation is also developed between the specific growth rate and the non-dimensional number. The modified exponential function predicted the FCGR within the acceptable values for all three stages in the radial direction. It shows the best performance for stage-I of FCGR and the lowest for stage-III. The microstructure envisages shallowed microvoids, while the striations and secondary cracks are mostly perpendicular to the FCG direction.

Keywords: exponential function, specific growth rate, fatigue crack, stress intensity factor, SDG 9

1. Introduction

Fatigue failure of steel pipes is one of the most important design criteria in pipeline engineering. The steel pipes are used to transport fluids in the petrochemical, aerospace, automobile, and chemical industries [1]. The change in pressure and external loading during service envisages a sinusoidal loading, which makes the steel pipes susceptible to fatigue failure [2]. Therefore, fatigue crack growth (FCG) is a vital failure phenomenon in pipeline steel due to the vibrational nature of fluid and operational environment [3]. It is quite possible that during a significant service time, a microcrack can be generated in the pipeline surface, which acts as a stress accumulator in its vicinity, and once threshold stresses accumulate, it results in FCG [4-5]. It is also possible that a new crack can generate and change the stress field locally, providing the required localized stresses for multiple/or new crack propagation. One of the driving forces in such failure is stress intensity. In general, the stress intensity is not defined for certain crack geometries (solid or tubular) of pipes, as the pipeline is not a standard geometry for fatigue crack experimentations and simulations [6-7]. The varying thickness of different pipes makes it even more difficult to consider different loading conditions and applications [8-9]. Also, the initial microcrack in pipes can be of part-through type or through-the-thickness dominant type, yet the crack propagation characteristics of such pipe geometries remain unknown.

* Corresponding author. E-mail address: kumarpawan@mail.ru

To address such phenomena of fatigue crack propagation in steel pipes, different FCG models were developed considering external sinusoidal load, the effect of inclusion, and the environmental effect [10-12]. These models were based on several approaches, including finite element analysis, mathematical modeling, and descriptive analysis. Teng An et al. calculated the FCG of X80 grades of pipeline steel, considering the hydrogen pressure [13]. They reported a reduced fatigue due to hydrogen-accelerated crack propagation. In a similar study, Fatoba et al. studied the low-cycle fatigue behavior of API5L X65 pipeline steel under completely reversed strain-controlled situations at ambient temperature and reported a decrease in fatigue life with increasing plastic strain amplitude [14]. Jiang et al. also reported that FCG is mostly dependent on stress intensity range and reported an increasing FCG [15]. In addition to fatigue load, Bonab et al. considered the influence of microstructure on FCG in API X65 pipeline steel. They studied a non-metallic inclusion and reported crack nucleation after a significant number of loading cycles [16]. In a similar work, the authors have also studied features of intergranular and trans-granular FCG and observed an accretion of Σ3 boundaries around the fatigue microcracks as high-energy boundaries [17]. Apart from external loading and inclusion, the environmental effect on FCG was also studied. Ronevich et al. considered the effect of microstructure banding on hydrogen-abetted FCG in X65 pipeline steels [18]. In a similar work, Slifka et al. also studied the influence of microstructure on the hydrogen-assisted FCG in pipeline steel and reported the effect of different microstructures, considering the emphasis on the low ΔK regime [19]. Igwemezie et al. also studied the influence of microstructure on FCGR in marine steels, considering the Paris region of FCG. The authors reported that the crack tip diversion, crack front bifurcation, and metal crumb formation affect the FCGR [20]. Sahu et al. predicted FCGR for TP316L stainless steel pipe in the circumferential direction [21]. However, they did not consider different stages of FCGR for modeling. It is believed that the fatigue failure in pipes is more significant in the radial direction and that a break-before-leak model is more relevant and practical for applications.

In earlier work, Kumar et al. used an exponential model, the gamma function, and finite element analysis to predict FCGR in TP316L stainless steel pipe specimens [22-24]. However, the modeling was carried out without considering the different stages of FCGR. Also, the prediction of the FCGR was only for the initial crack propagation. The model did not address the FCGR when the crack propagation was accelerated with the number of cycles. Therefore, it is still unknown whether the FCGR is in accelerated stages, and the corresponding modeling formulation has yet to be defined. Further, they did not address the microstructural features of the fatigue-fracture surfaces. Hence, it is believed that a more comprehensive analysis and modifications are required so that the FCGR can be predicted not only for the initial stage but also for all three stages of FCG. The relationship between the specific growth rate and the non-dimensional number also needs to be addressed. The effect of stress accumulation on the fatigue-fracture surface features also needed to be analyzed. Therefore, in the present work, a modified exponential model is developed for fatigue crack propagation in through-the-thickness pipe walls to predict the FCGR in all three distinct stages. A relationship between a specific growth rate and the non-dimensional number is established. The predicted model is validated through the experimental data obtained from a four-point bending test conducted at ambient temperature. The performance of the model is analyzed using statistical methods like mean absolute error (MAE), mean squared error (MSE), root mean square error (RMSE), mean prediction ratio (MPR), mean % deviation, and coefficient of determination (R^2), followed by error band scatter analysis. The microstructural features of the fatigue-fractured surface are studied using standard microscopy characterization.

2. Materials and Methodology

The TP316L stainless steel pipe was deformed to large-scale plastic deformation under pure bending using a servo-hydraulic dynamic testing apparatus (Instron 8800). The four-point bending test setup and the pipe specimen with a centrally attached crack opening displacement (COD) gauge on a servo-hydraulic universal testing apparatus (Instron 8800) are shown in Fig. 1 [22-23]. However, the representation of the cross-sectional view of the pipe specimen and constant amplitude loading

condition is shown in Fig. 2 and Fig. 3, respectively. The specimen dimensions exhibiting inner radius, outer radius, thickness (in the radial direction), span of the support rollers, span of the load rollers, and the end clearance are presented in Table 1. The mechanical properties of the TP316L stainless steel are presented in Table 2.

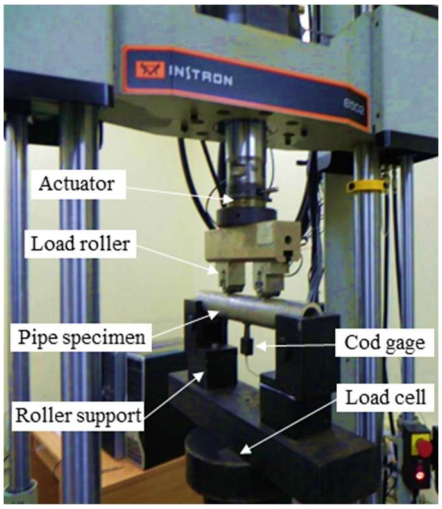

Fig. 1 Four-point bending test setup

The four-point bending test was conducted considering a sinusoidal load of 22.5 *k*N, a stress ratio of 0.1, and a frequency of 4 Hz was applied to the specimen. The four-point bending test was conducted at ambient temperature. The distance of the load line and reaction force was 110 mm and 225 mm, respectively, from the center of the pre-notch. The pre-notch had a semi-elliptical geometry with the length of the major axis 22.96 mm, and the semi-minor axis (in the radial direction of the pipe)-2.28 mm.

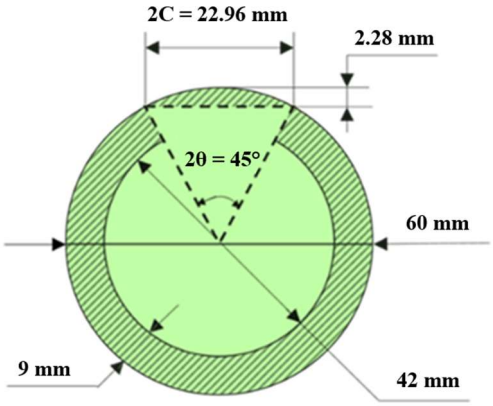

Fig. 2 Cross-sectional view of the pipe specimen

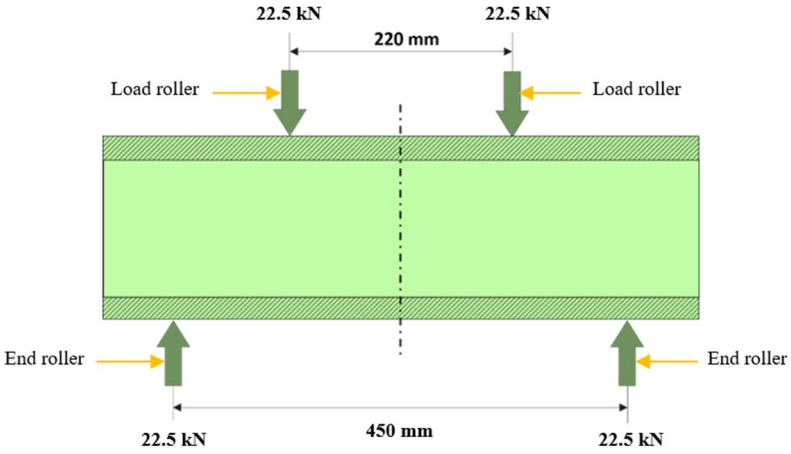

Fig. 3 Constant amplitude loading condition in four-point bending

The FCG data in terms of crack length (a) and number of loading cycles (N) was monitored using a crack opening displacement (COD) gauge and processor. The COD gauge was mounted at the crack mouth with suitable knife edges. Since there is no direct crack-compliance correlation available for the measurement of the FCG in part-through cracked pipes, the COD gauge was calibrated to find the correlation between radial crack lengths and ΔCOD output [22-23]. The calibration curves thus obtained have been utilized for the indirect measurement of the crack lengths in the radial direction. The microstructural characterization of the fatigue-fractured pipe specimen was carried out using a JEOL JSM-6480 LV scanning electron microscope (SEM). The samples for SEM analysis were prepared as per the regular metallographic procedures. The mounted samples were mechanically polished using the emery papers with grit levels ranging from 100-500 μm, followed by cloth polishing using a TEGRAPOL polishing apparatus. The polishing grit in the size sequence of 9 μ, 3 μ, and 1 μ was used for mechanical polishing.

Table 1 Specimen dimensions [22-23]

Outer radius (R_o)	Inner radius (R_i)	Thickness (t)	Span of the support rollers	Span of the load rollers	End clearance
30mm	21mm	9 mm	450 mm	220 mm	25 mm

Table 2 Mechanical properties of TP 316L stainless steel [22-23]

Material	Modulus of Elasticity (E)	Poisson's ratio (μ)	Yield strength (σ_{YS})	Ultimate tensile strength (σ_{ut})
316L Stainless steel	220 GPa	0.3	366 MPa	611 MPa

3. Results and Discussion

This section describes the stress intensity factor and its influence on crack propagation. The fatigue crack growth rates in stages- I, II, and III are defined. The modelling of FCGR for all three stages is formulated with a modification to the exponential function. It is then followed by a performance evaluation and comparison with earlier developed models. The microstructural features are discussed to characterize fatigue crack propagation.

3.1. Stress intensity factor and crack propagation

The FCG data was generated using the Instron 8800 apparatus. The increase in a with N was recorded. The stress intensity factor (K), considering the mean of 5 specimens under pure bending, with corresponding a and N, is shown in Fig. 4. The theoretical K indexes the pre-notch stress field singularity by delineating the stress field in the vicinity of the pre-notch where the singularity occurred. In other words, K predicted the state of stress near the vicinity of the pre-notch (which was at the center of the specimen with a semi-elliptical geometry). The theoretical K depends on the geometry of the crack, the geometry of the specimen, structural constraints, and loading conditions. The K was calculated using the methodology provided by Laham et al. [25]. The geometrical functions (f_t and f_{bg}) were extra-plotted for the pipe specimen and elliptical crack geometries. The theoretical K is given by Eq. (1).

$$K = \sqrt{\pi a}\left(\sum_{i=1}^{3}\sigma_t \times f_t \times \frac{a}{t} \times \frac{2c}{a} \times \frac{R_i}{t} + \sigma_{bg} \times f_{bg} \times \frac{a}{t} \times \frac{2c}{a} \times \frac{R_i}{t}\right) \quad (1)$$

where σ_{bg} is bending stress, σ_t is axis-symmetrical stress (zero in the current case), a is the depth of the elliptical defect/length of the semi-minor axis, t is the thickness of the pipe, $2c$ is the length of the major axis, and R_i is the internal radius of the pipe. The first computable a of 0.87 mm was detected at a loading cycle of 60530. In the current work, the N for the first appearance of a was considered as the start of the loading cycle. This premise was considered for plastic behavior and eliminated all linear

elastic deformation. Fig. 4(a) describes variation in K with a. The curve shows a typical K-a variation for FCG [26]. The slope of the curve decreases with the a continuously. In other words, initially, for a small increment in a, the corresponding increase in K was greater. For further crack propagation, the slope decreases, which means a lower incremental K was required for the corresponding increment in a. Therefore, it envisages a preceding crack that changes the stress field near the vicinity of the crack tip, and envisages a new crack to be less resistant to external bending [27]. This nature continued till the complete failure of the sample.

It is to be noted that the slope of the K-a curve after a preceding crack length of 4 mm decreased significantly as compared to the slope at the initiation of the crack (when a=0.85 mm). The variation in K with N is shown in Fig. 4(b). The nature of the plot shows a typical K-N curve [28]. In contrast to the K-a curve, the slope of the K-N curve increases continuously till the fracture. Initially, a higher N is required for a small increase in K, which indicates that the initial crack propagation required a large accumulation of external bending stresses (using higher N). With the crack propagation and accumulation of external bending stresses, the subsequent requirement of N for an incremental K decreased. It is suggested that the preceding bending stress accumulation made the crack tip more susceptible to propagating (growing). A much higher slope of the K-N curve after N reaches 60,000 envisages a highly plastic deformation state, which eventually leads to the fracture of the specimen.

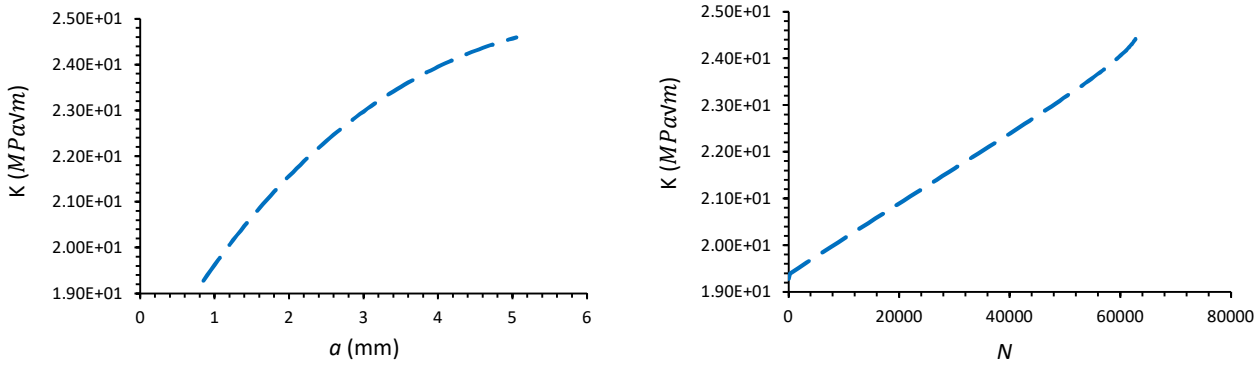

(a) K vs a graph (b) K vs N graph

Fig. 4 The variation in K with a and N

3.2. FCGR

The FCGR provides the features of crack propagation. It is the rate of change of a with N; in other words, it provides an idea of incremental a in a given interval of N. The variations of da/dN with ΔK, a, and N are presented in Figs. 5, 6, and 7, respectively. Based on the nature of FCGR, it is categorized into three discrete stages: stage-I, stage-II, and stage-III for the present investigation. The three distinct stages characterize FCGR.

3.2.1. FCGR in stage-I

As shown in Fig. 5, the stage-I of FCGR is in the threshold ΔK range 17.45-20.46 $MPa\sqrt{m}$. The appearance of the first crack is observed at ΔK =17.45 $MPa\sqrt{m}$, and the slope increases gradually up to ΔK =20.46 $MPa\sqrt{m}$. The initiation of the first crack required a critical accumulation of bending stresses near the vicinity of the crack tip, which was provided by the threshold ΔK [29]. The da/dN versus ΔK curve is detrimental to FCG studies [27]. The ΔK provided the driving force for FCG, which is proportional to applied bending stress and the square root of a (equation 1). The slowly increasing slope of the da/dN versus ΔK curve in stage-I envisages that a higher crack driving force was required initially. This is the region where the crack resisting parameter (K_c) and materials property (stiffness, E) oppose the crack driving force (ΔK) at best after the threshold ΔK. It required a higher ΔK for a small increment in the da/dN. The FCGR versus a curve is shown in Fig. 6.

The stage-I of FCGR is in the crack length, *a,* range of 0.8-2.8 mm. It is observed that the slope of d*a*/d*N* versus *a* curve increases gradually, indicating that a higher number of loading cycles is required for a small increment in crack length in the region. The same is also evident from the d*a*/d*N* versus *N* curve, shown in Fig. 7. The range of *N* for stage-I of FCGR is observed between 0-44419, in the plastic region.

3.2.2. FCGR in stage-II

From Fig. 5, the stage-II of FCGR is observed in the Δ*K* range 20.46-21.41 $MPa\sqrt{m}$. IN this range, the slope of d*a*/d*N* versus Δ*K* increases significantly. In other words, the crack driving force Δ*K* decreases with increasing *a*. It is suggested that the bending stress accumulation in the previous stage played a significant role in reducing the required drive force for FCG. It indicates that the crack softening accelerates as compared to the previous stage. The increasing slope of FCGR between 2.8-4.15 mm envisages that a comparatively lower number of *N* was required for a corresponding increase in *a* as compared to stage-I, as shown in Fig. 6. The hypothesis of the lower *N* was confirmed from the slopes of FCGR versus *N* in stage-II, as shown in Fig. 7. The *N* for stage-II of FCGR was from 44419-60106.

3.2.3. FCGR in stage-III

The stage-III of FCGR showed an accelerated crack growth. The slope of d*a*/d*N* versus Δ*K* increased vigorously. It means, the driving force required for an existing crack (in the previous stage-II) to propagate was highly reduced, and an accelerated FCG occurred with a lower increase in Δ*K*. As shown in Fig. 5, the stage-III of FCGR is in the Δ*K* range 21.41-21.98 $MPa\sqrt{m}$. As shown in Figs. 6 and 7, a much lower number of loading cycles was required for a corresponding crack propagation and hence, d*a*/d*N* increases rapidly for a given *a* and *N*. It is suggested that in this region, the crack driving force (Δ*K*) was subjugated to the crack resisting parameter (K_c) and material properties (stiffness, *E*). The stage-III was characterized in the *a* range4.15-4.75 mm and a corresponding *N* 60106-63014. After a Δ*K* of 21.98 $MPa\sqrt{m}$, *a* of 4.75 mm, and *N* 63014, the FCGR is highly accelerated, and the material reaches the tri-axial stresses envisaging necking phenomena that eventually led to the catastrophic failure of the material [21, 27].

The next stage of FCG after 4.75 mm of crack length (which was 7.03 mm considering the pre-notch length) up to the radial thickness of pipe (equal to 9 mm) was not considered for FCGR modelling due to the limitation of the modified exponential function, stress-triaxiality in the vicinity of crack, and requirement of complex mathematical expressions. Based on the above discussion, the boundary conditions and FCGR for all three stages are shown in Table 3.

Table 3 Boundary conditions and FCGR for all three stages

Stage of FCGR	Boundary condition	Phenomena of FCGR
I	$FCGR_{\text{stage-I}} = a\left[0.85\,mm, 2.80\,mm\right]; \Delta K\left[17.45MPa\sqrt{m}, 20.46MPa\sqrt{m}\right]$	The cracks resisting parameter (K_c) and materials property (stiffness, *E*) oppose the crack driving force (Δ*K*) at best after the threshold Δ*K*.
II	$FCGR_{\text{stage-II}} = a\left[2.80\,mm, 4.15\,mm\right]; \Delta K\left[20.46MPa\sqrt{m}, 21.41MPa\sqrt{m}\right]$	The driving force Δ*K* was decreased with increasing *a*.
III	$FCGR_{\text{stage-III}} = a\left[4.15\,mm, 4.75\,mm\right]; \Delta K\left[21.41MPa\sqrt{m}, 21.98MPa\sqrt{m}\right]$	The driving force (Δ*K*) was subjugated to the crack resisting parameter (K_c) and material property (stiffness, *E*).

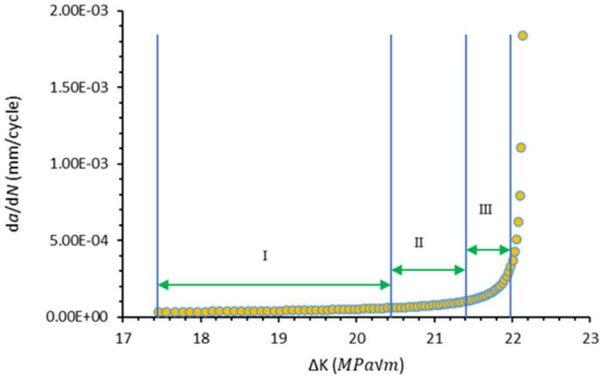

Fig. 5 FCGR versus ΔK for stages-I, II, and III

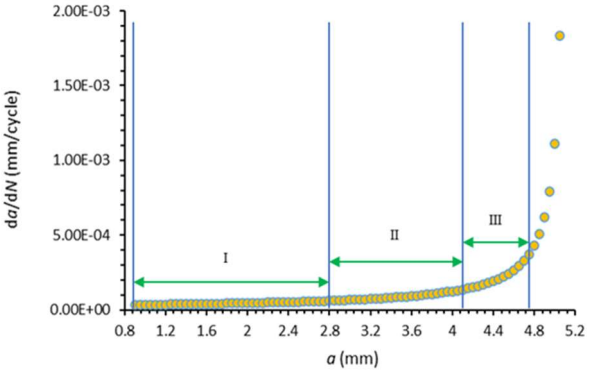

Fig. 6 FCGR versus a for stages-I, II, and III

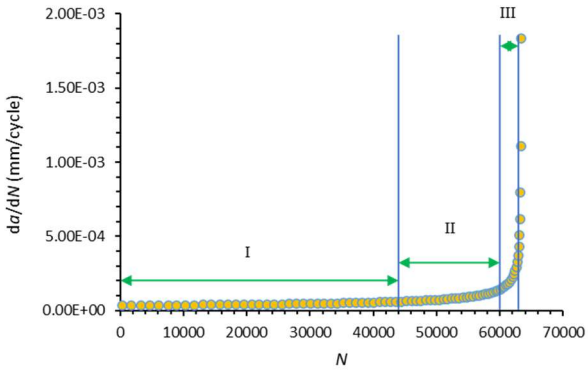

Fig. 7 FCGR versus N for stages-I, II, and III

4. Modelling of FCGR Using a Modified Exponential Function

The model considered the crack driving force and crack resisting parameters to characterize the nature of da/dN and then predicted the FCGR. The specific growth rate is discussed for all the stages. Then, the modifications made to the exponential function are discussed.

4.1 Formulation of the modified exponential function

The hypothesis of a given mathematical function is proportional to the speed at which the function rises, as defined by the exponential function given below

$$P(t) = P_o e^{rt} \tag{2}$$

where P is population, P_o is the initial population, t is the time, and the quantity r in the above equation is the Malthusian parameter or specific growth rate. The Eq. (1) has been modified by Kumar et al. to calculate a for a given N. The modified equation can be obtained by [22-23].

$$a_j = a_i e^{m_{ij}} (N_j - N_i) \tag{3}$$

where, for a given interval (i, j), a_j is the final crack length, a_i is the initial crack length, $N_j - N_i$ is the load cycle interval, and m_{ij} is the specific growth rate. The m_{ij} can be calculated by

$$m_{ij} = \frac{\ln\left(\frac{a_j}{a_i}\right)}{N_j - N_i} \tag{4}$$

In the present work, the specific growth rate m_{ij} is modified and correlated with a non-dimensional number n as given in Eq. (5)

$$m = An^2 + Bn + C \tag{5}$$

where n was correlated with two crack driving forces, ΔK and maximum stress intensity factor (K_{max}), as well as material parameters, fracture toughness (K_c), stiffness (E), and Yield stress (σ_{YS}). The above equation has been modified to a 2nd degree polynomial for the present study. However, in the previous exponential model, it was a 3rd degree polynomial. In the present work, the modified non-dimensional parameter n can be represented by

$$n = \frac{\Delta K}{K_C} \times \frac{K_{max}}{K_C} \times \frac{\sigma_{YS}}{E} \tag{6}$$

The above equation has been modified as a monomial. However, in the previous exponential model, it was an equation with a fractional power of 0.25. The constants (A, B, and C) were calculated for stages-I, II, and III of FCGR and the subsequent m_{ij} and the predicted number of loading cycles (N_j^P) can be calculated by

$$N_j^P = \frac{\ln\left(\frac{a_j}{a_i}\right)}{m_{ij}} + N_i \tag{7}$$

4.2 Calculation of m_{ij} and the curve fitting constant for stages- I, II, and III of FCG

The specific growth rate m_{ij} defined in Eq. (4) was plotted with the non-dimensional number n (defined in Eq. (6)). This graph provided the relationship between FCG characteristics with crack driving force and material properties. The curve was fitted with a polynomial equation (given in Eq. (5) for stages-I, II, and III of FCGR. The curve-fitting constants are presented in Table 4. Figs. 8, 9, and 10 provide the variation of the specific growth rate with the crack driving force and crack resistive parameters. In stage-I of FCGR (Fig. 8), the decreasing slope envisages the emancipation of the combined effect of crack driving force and crack resistance parameter. This suggests that the crack propagation was slow with the N during the initial stage of FCG. However, once a sufficient amount of stress intensification near the vicinity of the crack tip occurred, the slope of specific crack growth rate versus non-dimensional number n increases as shown for stages-II and III of FCGR in Figs. 9 and 10. Such an increase depicts the dominance of the effect of the crack driving force over the crack resistance parameters. It also indicated an accelerated crack propagation with the number of N. The different natures of the slopes in stages-I, II, and III characterized the nature of FCG in the respective stages.

Table 4 Curve fitting constants for stages-I, II, and III of FCG

Stage of FCG	A	B	C
stage-I	7989107.2800	−91.4011	0.0002
stage-II	33838863.5100	−413.1787	0.0012
stage-III	1116368244.00	−15001.6072	0.0504

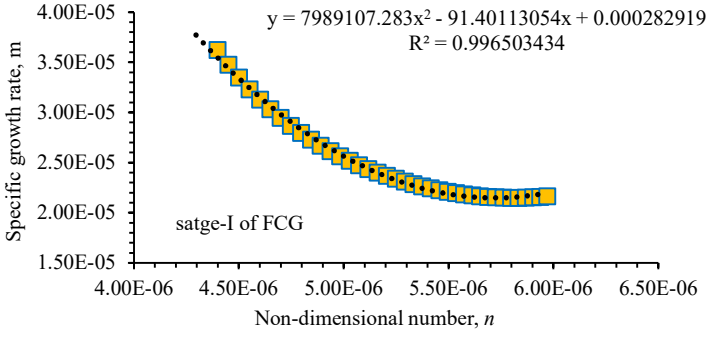

Fig. 8 Specific growth rate versus n for stage-I of FCG

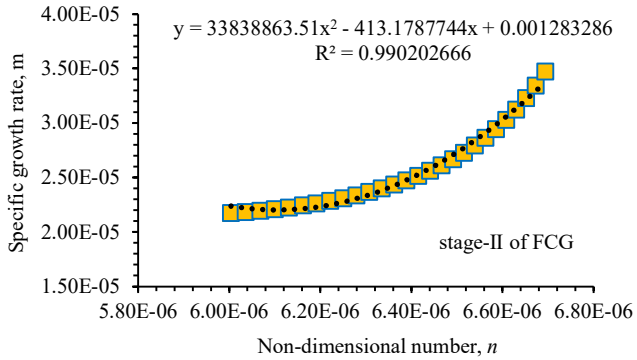

Fig. 9 Specific growth rate versus *n* for stages-II of FCG

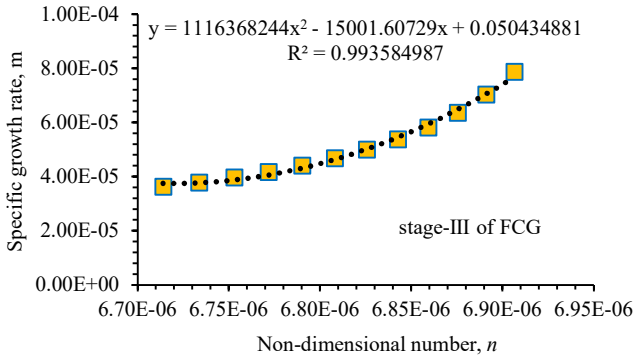

Fig. 10 Specific growth rate versus *n* for stage-III of FCG

4.3 Prediction of FCGR using a modified exponential function and specific growth rate

The modified exponential function and specific growth rate were formulated considering the experimental data of 5 samples, followed by validation of the model using the 6th sample. The N was predicted using Eq. (7), and then the values of da/dN were calculated. The FCGR was plotted against ΔK for stages-I, II, and III as shown in Figs. 11, 12, and 13, respectively.

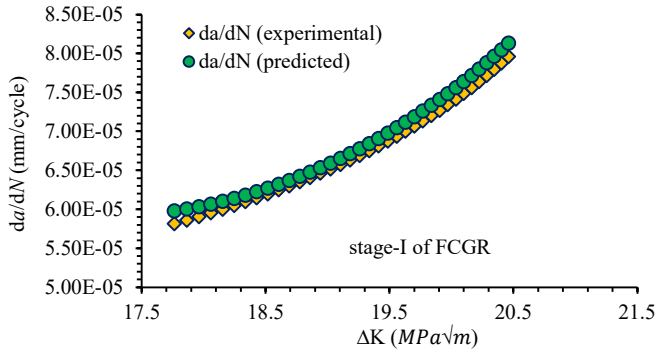

Fig. 11 FCGR in stage-I

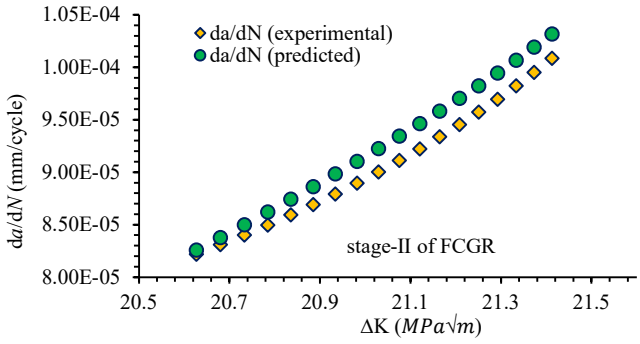

Fig. 12 FCGR in stage-II

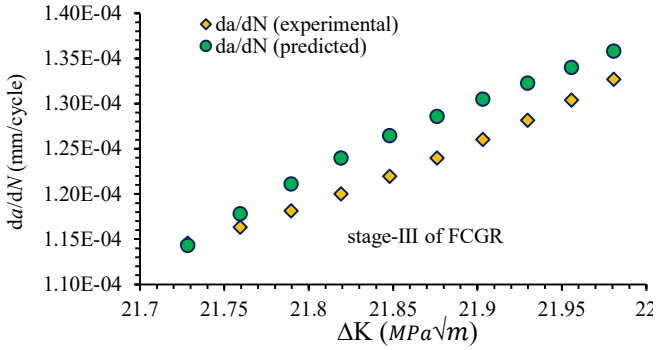

Fig. 13 FCGR in stage-III

The modelling agreed with the experimental data. However, the accuracy and performance studies of the model required statistical analysis for quantification. It is also observed that the predicted FCGR in all three stages provided a higher value as compared to the experimental data. In other words, the model overestimates the materials' properties and geometry.

4.4 Modification in the exponential function

In the previous work, the non-dimensional parameter n is defined as [22]:

$$\underbrace{n}_{\text{earlier model}} = \left[\frac{K}{K_C} \times \frac{K_{\max}}{K_C} \times \frac{\sigma_{YS}}{E}\right]^{0.25} \tag{8}$$

However, in the present work, the formulation of the non-dimensional number has been modified. One of the crack driving forces used in the previous work was stress intensity (K). However, it was felt that, rather than K, it was the stress intensity change (ΔK) that provided the crack driving force for distinct stages of FCGR. Also, the exponent 0.25 was changed to 1. Therefore, the modified non-dimensional parameter n can be computed by

$$\underset{\text{modified model}}{\underset{\sim}{n}} = \frac{\Delta K}{K_C} \times \frac{K_{\max}}{K_C} \times \frac{\sigma_{YS}}{E} \tag{9}$$

Another modification introduced was the correlation between the specific growth rate m and the non-dimensional number n. In the previous work, the correlation can be calculated using the 3-degree polynomial below [22]:

$$\underset{\text{earlier model}}{\underset{\sim}{m}} = An^3 + Bn^2 + Cn + D \tag{10}$$

However, in the current work, the correlation can be computed by

$$\underset{\text{modified model}}{\underset{\sim}{m}} = An^2 + Bn + C \tag{11}$$

One of the modifications done in the present work is to predict the FCGR in a wider range for the through-the-thickness direction of the pipe. The limits of the earlier model and the modified model are presented as

$$\lim_{0.85\ mm\ -\ 2.95\ mm} crack\ length\ \overrightarrow{modified\ model} \lim_{0.85\ mm\ -\ 4.75\ mm} crack\ length \tag{12}$$

$$\lim_{17.45 MPa\sqrt{m} - 20.62 MPa\sqrt{m}} \Delta K\ \overrightarrow{modified\ model} \lim_{17.45 MPa\sqrt{m} - 21.98 MPa\sqrt{m}} \Delta K \tag{13}$$

4.5 Performance of model

The performance of the model was analyzed using statistical methods like mean absolute error (MAE), mean squared error (MSE), root mean square error (RMSE), mean prediction ratio (MPR), mean % deviation, and coefficient of determination (R^2). The different statistical methods are expressed as

$$MAE = \frac{1}{n}\sum_{i=1}^{n} \{experimental\ data\}_i - \{predicted\ value\}_i \tag{14}$$

$$MSE = \frac{1}{n}\sum_{i=1}^{n} \left(\{experimental\ data\}_i - \{predicted\ value\}_i\right)^2 \tag{15}$$

$$RMSE = \sqrt{MSE} \tag{16}$$

$$MPR = \frac{1}{n}\sum_{i=1}^{n} \frac{(experimental\ data)_i}{(predicted\ value)_i} \tag{17}$$

$$Mean\%\ deviation = \frac{1}{n}\sum_{i=1}^{n} \frac{\{\exp erimental\ data\}_i - \{predicted\ value\}_i}{\{\exp erimental\ data\}_i} \times 100 \tag{18}$$

$$R^2 = 1 - \frac{sum\ of\ square\ error}{sum\ of\ squares\ total} \tag{19}$$

The quantitative analysis of the model is shown in Table 5. The model showed the lowest (and the best) value of MAE, MSE, and RMSE for stage-I of FCGR and the highest for stage-III. However, the performance of the model was within the acceptable values for all three stages. For stages-I and II, modelling provided the best results; however, for stage-III, modelling was comparatively conservative, but still in the acceptable range. It is suggested that the modified exponential function and specific growth rate depict the slopes of da/dN versus the ΔK curve precisely, where the FCGR was initially slow during stage-I and accelerated during stage-II. When the crack FCGR was highly accelerated, the model depicted a fall in the performance.

The MPR, mean % deviation, and R^2 in stage-I of FCGR showed the best performance. An R^2 of 0.998 and 0.997 in stages-I and II indicated that the hypothesis of the use of a modified exponential function and specific growth rate to predict the FCGR agreed with the experimental outcomes. The performance of the model dropped to a value of 0.969 for R^2 in stage-III of FCGR. When the FCGR was highly accelerated, the modified exponential function became conservative and showed a lower performance as compared to stages-I and II. A mean prediction ratio of <1 for all three stages of FCGR depicted that the model performance was on the higher side of the experimental data. In other words, the predicted values of da/dN were greater than the experimental values.

Table 5 Performance of the model for the prediction of FCGR as a function of ΔK

Stage of FCGR	MAE	MSE	RMSE	MPR	Mean % deviation	R^2
stage-I	1.13812E−06	1.41535E−12	1.18969E−06	0.983	1.664	0.998
stage-II	1.9169E−06	4.12088E−12	2.02999E−06	0.979	2.075	0.997
stage-III	3.30524E−06	1.27444E−11	3.56993E−06	0.974	2.655	0.969

The error band scatter analysis was carried out for the predicted and experimental results of FCGR for stages-I, II, and II. The results of the analysis are shown in Figs. 14, 15, and 16, respectively. The error band scatter was considered on the positive side of the perfect fit because the predicted values were on the higher side of the experimental data. The error band for stages-I, II, and III falls on the positive side by 0.034, 0.035, and 0.043 % of the perfect fit.

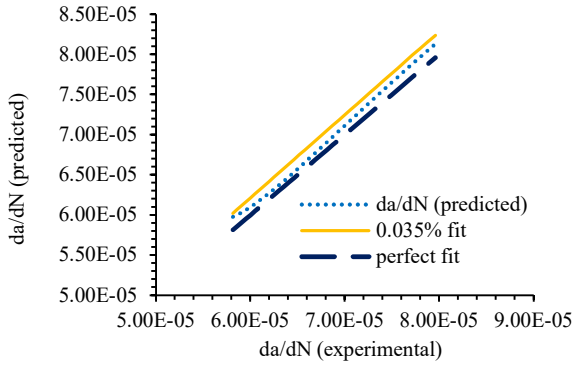

Fig. 14 Error band scatter for stage-I of FCGR

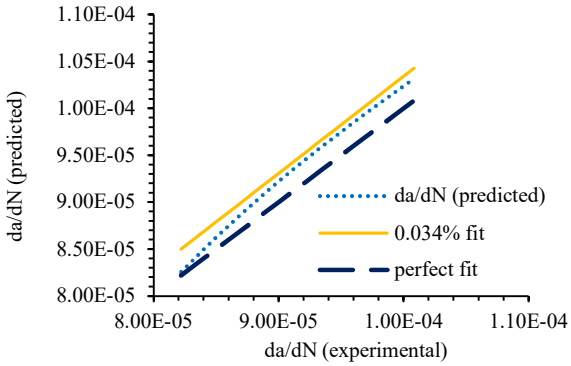

Fig. 15 Error band scatter for stage-II of FCGR

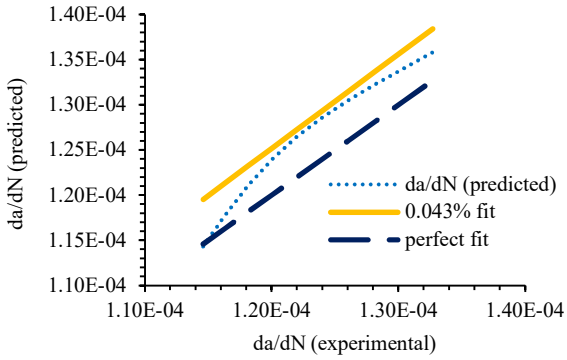

Fig. 16 Error band scatter for stage-III of FCGR

4.6 Comparison of the performance of the model with earlier developed models

The performance of the modified exponential function in the present work was compared with previous models developed in earlier work [22]. The earlier models only predicted FCGR for stage-I. Although the present work predicted FCGR for all three stages, only the stage-I of FCGR prediction performance has been compared and presented in Table 6. There was a significant advancement in the performance observed for the modified exponential function as compared to the earlier

exponential model for MAE, MSE, RMSE, MPR, and mean % deviation. However, the coefficient of determination (R^2) was similar for both models. On the other hand, in comparison with the gamma mode [23], the gamma function performed marginally better for MAE, MSE, and RMSE performance and significantly better for mean % deviation, while the MPR and R^2 were similar to the current work's model.

Table 6 Performance of the model

Model type	MAE	MSE	RMSE	MPR	Mean % deviation	R^2
Modified exponential function	1.13812E−06	1.41535E−12	1.18969E−06	0.983	1.664	0.998
Earlier exponential model	9.07E−06	8.14E−11	9.02E−06	0.83	10.14	0.995
Gamma function	1.23113E−06	1.88896E−12	1.37439E−06	0.99	0.30	1.02

For the specific grades of material and loading conditions used in the present work, the dataset is not available for comparison with models developed by other researchers. Hence, the modified exponential function discussed here was compared with the Paris equation [20]. The stage-II of any FCG curve depicts the Paris region and its law. Therefore, the modified exponential function was compared for this stage specifically. The Paris curve fitting is shown in Fig. 17. The curve fitting equations given in red and green colors, in Fig. 17, represent the experimental and modified exponential model, respectively. The materials constants (C and n) are obtained using Eq. (20), and the goodness of fit is presented in Table 7.

$$\frac{da}{dN} = C\Delta K^n \tag{20}$$

where C and n are material constants that depend upon the environment, frequency, temperature, and stress ratio. The a and N are crack length and number of cycles, respectively.

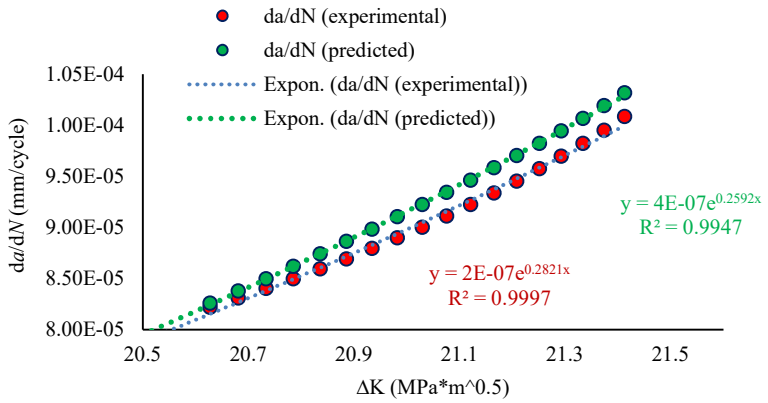

Fig. 17 FCGR curve in the Paris region

Table 7 Constants of the Paris equation and goodness of fit

Type of model	C	n	Goodness of fit
Modified exponential function	4E-07	0.2592	0.994
Paris model	2E-07	0.2821	0.999

5. Microstructure Analysis

The image of the fatigue-fracture cross-section of the pipe specimen is shown in Fig. 18. The green, blue, and black arrow indicates the pre-notch, fatigue-fractured surface, and machined part, respectively. A granular microstructure (indicated by blue arrow), which is completely different from the non-fatigue surface, is observed. The granular surface morphology characteristics of the fatigue-fractured surface were in line with earlier reports [27]. It is suggested that the ΔK provides the necessary crack driving force. FCG microstructural fractography features envisage the crack growth mechanism of the material due to the stress accumulation on the surface for a given N. The FCG microstructural features are characteristics of pure

bending and the initial microstructure of the material [27]. In the case of pipeline steel, the FCG wear was influenced by the formation of surface and sub-surface cracks after sufficient plastic deformation led to severe damage. The surface wear was characterized by the method of crack propagation, which was induced by plastic deformation, envisaging the amendment of the microstructure of the fractured surface, distressing the FCG wear procedures.

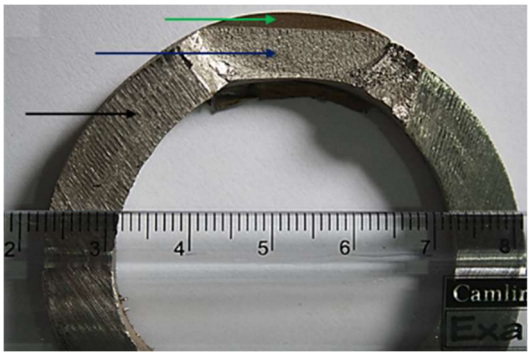

Fig. 18 The image of the fatigue-fracture cross-section

The SEM microstructure is shown in Fig. 19. It is suggested that these crack initiation sites were generated during the FCG test once a sufficient crack driving force (ΔK) was achieved. The crack driving force then provides sufficient energy to generate dislocations in grain interiors. Similar phenomena were reported by Kung et al., stating that the preliminary FCG cracks were generated in the grain interior [27]. These dislocations are then converted into microvoids with increasing *N* as shown in Fig. 19(a). Several microvoids were generated, suggesting high-energy sites. It was also observed that these microvoids were shallowed, indicating an acceleration in crack growth. The microstructural features, including striations and secondary cracks, were also observed as shown in Figs. 19(b) and (c), respectively. Moving along the radial direction towards the inner surface of the pipe, the striations were perceived at a few locations. These striations were mostly oriented upright to the FCG direction and close to the inner wall of the pipe.

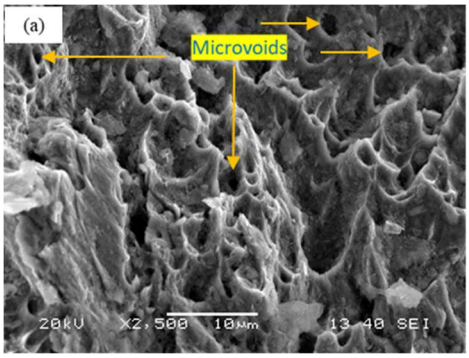

(a) Microvoids

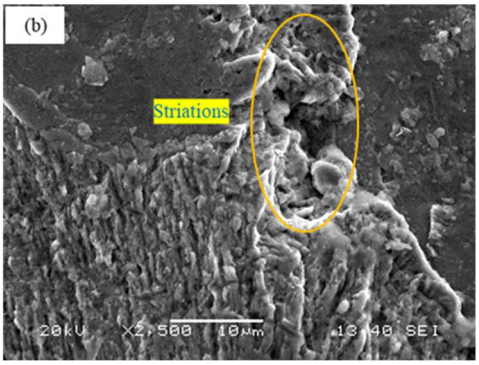

(b) Striations

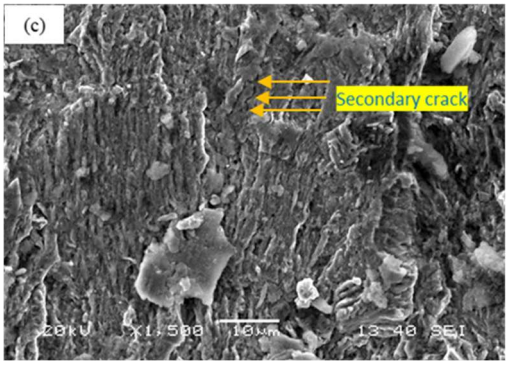

(c) Secondary crack

Fig. 19 Microstructure of fatigue-fractured surface

It is suggested that these striations envisage the parting of damage accumulation and crack-tip fracture steps for crack advancement as an outcome of continuous cyclic loading [27]. The section on strain accumulation influences the critical boundary and is well-thought-out, the feeble point at which the FCG initiation took place. It is suggested that the FCG crack spreads along the orientation of the feeble planes or dislocation cell boundaries, principal to the formation of the primary crack. The primary crack, on further strain accumulation, develops into the secondary cracks as shown in Fig. 19(c). These secondary cracks are designed on the sub-surface of the specimen and bend along the weaker plane near the surface.

6. Conclusions

An exponential fatigue crack growth model was developed using a modified specific growth rate for three distinct stages of FCGR for TP 316L stainless steel pipe. The model was validated through a comparative study of predicted results against experimental data. The performance of the proposed model was analyzed using statistical methods. The following are the important conclusions drawn from the present study:

(1) The specific growth rate in the modified form of $m_{ij} = A\left[\frac{\Delta K}{K_C}\times\frac{K_{\max}}{K_C}\times\frac{\sigma_{YS}}{E}\right]^2 + B\left[\frac{\Delta K}{K_C}\times\frac{K_{\max}}{K_C}\times\frac{\sigma_{YS}}{E}\right]^1 + C$ simulated the crack driving force and crack resistive parameters in all three stages with different curve fitting constants. Additionally, the modified exponential function in the form of $a_j = a_i^{m_{ij}}(N_j - N_i)$ predicted the da/dN with a given ΔK in stages-I, II, and III of FCGR.

(2) Stage-I of FCGR was from the threshold SIF range (17.45 $MPa\sqrt{m}$) to the value of ΔK (20.46 $MPa\sqrt{m}$), up to which FCGR slope was increasing slowly. Stage-II of FCGR was ΔK range 20.46-21.41 $MPa\sqrt{m}$, which was the stage where the slope of da/dN versus ΔK was significantly increased.

(3) In stage-III of FCGR, the driving force required for an existing crack (in stage II) to propagate was reduced significantly, and an accelerated crack propagation occurred with a lower increase in ΔK. Stage-III of FCGR was for the ΔK range 21.41-21.98 $MPa\sqrt{m}$.

(4) The model showed the lowest (also the best) value of MAE, MSE, and RMSE for stage-I of FCGR and the highest value for stage-III. The MPR, mean % deviation, and R^2 in stage-I of FCGR showed the best performance. The performance of the model dropped to a value of 0.969 for R^2 in stage-III of FCGR. The error band scatter for stages-I, II, and III falls on the positive side of the perfect fit.

(5) The microstructural features envisage striations and secondary cracks; while moving along the radial direction towards the inner surface of the pipe, the striations were perceived at a few locations. These striations were mostly preoccupied with being upright to the FCG direction and close to the inner wall of the pipe.

Acknowledgment

The authors wish to acknowledge The State Scientific Institution—The Joint Institute of Mechanical Engineering of The National Academy of Sciences of Belarus.

Funding

This work was carried out with the support of The Belarusian Republican Foundation for Fundamental Research (project number: T23RNF-125) and The Russian Science Foundation (grant number: 23-49-10061).

Conflicts of Interest

The authors declare no conflict of interest.

References

[1] J. Wanjun, W. Jinfu, N. Cunhou, and P. Xiaofei, "Application of Austenitic Stainless Steel Pipe in Petrochemical Units," Petroleum Refinery Engineering, vol. 53, no. 9. pp. 35-37, 2023.

[2] S. Vishnuvardhan et al., "Fatigue Ratcheting Studies on TP304 LN Stainless Steel Straight Pipes," Procedia Engineering, vol. 2, no. 1, pp. 2209-2218, 2010.

[3] A. B. Radwan, A. M. Abdullah, H. J. Roven, A. M. Mohamed, and S. K. Mobbassar Hassan, "Failure Analysis of 316L Air Cooler Stainless Steel Tube in a Natural Gas Production Field," International Journal of Electrochemical Science, vol. 10, no. 9, pp. 7606-7621, 2015.

[4] M. Puiggali, S. Rousserie, and M. Touzet, "Fatigue Crack Initiation on Low-Carbon Steel Pipes in a Near-Neutral-pH Environment Under Potential Control Conditions," Corrosion, vol. 58, no. 11, 2002.

[5] X. Guo, D. Zhang, and J. Zhang, "Detection of Fatigue-Induced Microcracks in a Pipe by Using Time-Reversed Nonlinear Guided Waves: A Three-Dimensional Model Study," Ultrasonics, vol. 52, no. 7, pp. 912-919, 2012.

[6] A. H. Noroozi, G. Glinka, and S. Lambert, "A Study of the Stress Ratio Effects on Fatigue Crack Growth Using the Unified Two-Parameter Fatigue Crack Growth Driving Force," International Journal of Fatigue, vol. 29, no. 9-11, pp. 1616-1633, 2007.

[7] A. H. Noroozi, G. Glinka, and S. Lambert, "Prediction of Fatigue Crack Growth under Constant Amplitude Loading and a Single Overload Based on Elasto-Plastic Crack Tip Stresses and Strains," Engineering Fracture Mechanics, vol. 75, no. 2, pp. 188-206, 2008.

[8] P. K. Singh et al., "Fatigue Studies on Carbon Steel Piping Materials and Components: Indian PHWRs," Nuclear Engineering and Design, vol. 238, no. 4, pp. 801-813, 2008.

[9] T. Hassan, M. Rahman, and S. Bari, "Low-Cycle Fatigue and Ratcheting Responses of Elbow Piping Components," Journal of Pressure Vessel Technology, vol. 137, no. 3, article no. 031010, 2015.

[10] H. Shirazi, S. Wang, W. Chen, and R. Eadie, "Pipeline Circumferential Corrosion Fatigue Failure under the Influence of Bending Residual Stress in the Near-Neutral pH Environment," Engineering Failure Analysis, vol. 166, pp. 108887, 2024.

[11] W. Liang, M. Lou, C. Zhang, D. Zhao, D. Yang, and Y. Wang, "Experimental Investigation and Phenomenological Modeling of Fatigue Crack Growth in X80 Pipeline Steel under Random Loading," International Journal of Fatigue, vol. 182, pp. 108169, 2024.

[12] Z. Lin et al., "The Dependence of Fatigue Property on Applied Stress in X80 Pipeline Steel Notched Specimens in Hydrogen Gas Environment," International Journal of Fatigue, vol. 183, pp. 108222, 2024.

[13] T. An, H. Peng, P. Bai, S. Zheng, X. Wen, and L. Zhang, "Influence of Hydrogen Pressure on Fatigue Properties of X80 Pipeline Steel," International Journal of Hydrogen Energy, vol. 42, no. 23, pp. 15669-15678, 2017.

[14] O. Fatoba and R. Akid, "Low Cycle Fatigue Behaviour of API 5L X65 Pipeline Steel at Room Temperature," Procedia Engineering, vol. 74, pp. 279-286, 2014.

[15] Y. Jiang and M. Chen, "Researches on the Fatigue Crack Propagation of Pipeline Steel," Energy Procedia, vol. 14, pp. 524-528, 2012.

[16] M. A. Mohtadi-Bonab, M. Eskandari, H. Ghaednia, and S. Das, "Effect of Microstructural Parameters on Fatigue Crack Propagation in an API X65 Pipeline Steel," Journal of Materials Engineering and Performance, vol. 25, no. 11, pp. 4933-4940, 2016.

[17] M. A. Mohtadi-Bonab, M. Eskandari, M. Sanayei, and S. Das, "Microstructural Aspects of Intergranular and Transgranular Crack Propagation in an API X65 Steel Pipeline Related to Fatigue Failure," Engineering Failure Analysis, vol. 94, pp. 214-225, 2018.

[18] J. A. Ronevich, B. P. Somerday, and C. W. San Marchi, "Effects of Microstructure Banding on Hydrogen-Assisted Fatigue Crack Growth in X65 Pipeline Steels," International Journal of Fatigue, vol. 82, pp. 497-504, 2016.

[19] A. J. Slifka et al., "The Effect of Microstructure on the Hydrogen-Assisted Fatigue of Pipeline Steels," Proceedings of American Society of Mechanical Engineers, Pressure Vessels and Piping Division (Publication) PVP, vol. 6, ASME Press, 2013.

[20] V. Igwemezie, A. Mehmanparast, and F. Brennan, "The Influence of Microstructure on the Fatigue Crack Growth Rate in Marine Steels in the Paris Region," Fatigue & Fracture of Engineering Materials & Structures, vol. 43, no. 10, pp. 2416-2440, 2020.

[21] V. K. Sahu, P. K. Ray, and B. B. Verma, “Experimental Fatigue Crack Growth Analysis and Modelling in Part-Through Circumferentially Pre-Cracked Pipes under Pure Bending Load,” Fatigue & Fracture of Engineering Materials & Structures, vol. 40, no. 7, pp. 1154-1163, 2017.

[22] P. Kumar, H. Patel, P. K. Ray, B. B.Verma, "Calibration of COD Gauge and Determination of Crack Profile for Prediction of Through the Thickness Fatigue Crack Growth in Pipes Using Exponential Function," Mechanics, Materials Science & Engineering, no. 9, 2016.

[23] P. Kumar, V. K. Sahu, P. K. Ray, B. B. Verma, "Modelling of Fatigue Crack Propagation in Part-Through Cracked Pipes Using Gamma Function," Mechanics, Materials Science & Engineering, no. 9, 2016.

[24] P. Kumar, M. E. Makhatha, S. Sengupta, and A. K. Dutt, “Prediction of the Propagation of Fatigue Cracks in Part-Through Cracked Pipes with CASCA and FRANC2D,” Transactions of the Indian Institute of Metals, vol. 73, no. 6, pp. 1417-1420, 2020.

[25] S. Al Laham and S. I. Branch, Stress Intensity Factor and Limit Load Handbook, vol. 3. British Energy Generation Limited, Gloucester, UK, 1998.

[26] A. Albedah, B. Bachir Bouiadjra, L. Aminallah, M. Es-Saheb, and F. Benyahia, “Numerical Analysis of the Effect of Thermal Residual Stresses on the Performances of Bonded Composite Repairs in Aircraft Structures,” Composites Part B: Engineering, vol. 42, no. 3, pp. 511-516, 2011.

[27] T. L. Anderson, Fracture Mechanics: Fundamentals and Applications, 4th ed. Boca Raton, FL: CRC Press, 2017.

[28] C. M. Roşca, Vâlcu ; Miriţoiu, “Fnk Model of Cracking Rate Calculus for a Variable Asymmetry Coefficient,” Acta Universitatis Cibiniensis, vol. 69, no. 1, pp. 72-81, 2017.

[29] W. F. Gale and T. C. Totemeier, Eds., Smithells Metals Reference Book, 8th ed. Butterworth-Heinemann, 2003.